The Astrophysical Journal Letters, 937:L40 (11pp), 2022 October 1 https://doi.org/10.3847/2041-8213/ac8d96
© 2022. The Author(s). Published by the American Astronomical Society.
OPEN ACCESS

Immediate Origin of the Moon as a Post-impact Satellite

J. A. Kegerreis[1,2], S. Ruiz-Bonilla[1], V. R. Eke[1], R. J. Massey[1], T. D. Sandnes[1], and L. F. A. Teodoro[3,4]
[1] Physics Department, Institute for Computational Cosmology, Durham University, Durham, DH1 3LE, UK; jacob.kegerreis@durham.ac.uk
[2] NASA Ames Research Center, Moffett Field, CA 94035, USA
[3] BAERI/NASA Ames Research Center, Moffett Field, CA 94035, USA
[4] School of Physics and Astronomy, University of Glasgow, G12 8QQ, Scotland, UK
Received 2022 July 1; revised 2022 August 23; accepted 2022 August 24; published 2022 October 4

Abstract

The Moon is traditionally thought to have coalesced from the debris ejected by a giant impact onto the early Earth. However, such models struggle to explain the similar isotopic compositions of Earth and lunar rocks at the same time as the system's angular momentum, and the details of potential impact scenarios are hotly debated. Above a high resolution threshold for simulations, we find that giant impacts can immediately place a satellite with similar mass and iron content to the Moon into orbit far outside Earth's Roche limit. Even satellites that initially pass within the Roche limit can reliably and predictably survive, by being partially stripped and then torqued onto wider, stable orbits. Furthermore, the outer layers of these directly formed satellites are molten over cooler interiors and are composed of around 60% proto-Earth material. This could alleviate the tension between the Moon's Earth-like isotopic composition and the different signature expected for the impactor. Immediate formation opens up new options for the Moon's early orbit and evolution, including the possibility of a highly tilted orbit to explain the lunar inclination, and offers a simpler, single-stage scenario for the origin of the Moon.

Unified Astronomy Thesaurus concepts: Lunar origin (966); Impact phenomena (779); Earth-moon system (436); Hydrodynamical simulations (767)

Supporting material: machine-readable table

1. Introduction

In the canonical hypothesis for the origin of the Moon, the early Earth is hit by a Mars-sized impactor, "Theia" (Hartmann & Davis 1975; Cameron & Ward 1976; Canup et al. 2021). The collision ejects a debris disk that can explain the Moon's large mass, angular momentum, and tiny iron core, but it creates a Moon derived mostly from impactor material (Canup & Asphaug 2001; Canup et al. 2021). This is a concern because the Moon has a near-identical isotopic composition to Earth for many elements (Meier et al. 2014; Melosh 2014; Lock et al. 2020), and it seems unlikely, though perhaps possible, that the impactor would already match the proto-Earth target's composition (Dauphas 2017; Mastrobuono-Battisti & Perets 2017; Schiller et al. 2018; Johansen et al. 2021). Additional equilibration after the impact could help but is probably insufficient (Pahlevan & Stevenson 2007; Nakajima & Stevenson 2015). However, some recent analysis suggests distinctly different oxygen isotopes with increasing depth in the lunar mantle (Cano & Sharp 2020), and hydrogen isotopes also indicate imperfect mixing between the proto-Earth and Theia (Desch & Robinson 2019).

The relative difference between the compositions of the resulting Moon (or protolunar disk) and Earth is often expressed by $\delta f_{\rm t} \equiv (f_{\rm t}^{\mathbb{C}}/f_{\rm t}^{\oplus}) - 1$, where $f_{\rm t}^{\mathbb{C},\oplus}$ is the mass fraction of each silicate reservoir that originated in the target (Reufer et al. 2012), such that $|\delta f_{\rm t}| < 10\%$ indicates very similar compositions and a pure-Theia lunar mantle would have $\delta f_{\rm t} = -100\%$.

Original content from this work may be used under the terms of the Creative Commons Attribution 4.0 licence. Any further distribution of this work must maintain attribution to the author(s) and the title of the work, journal citation and DOI.

Alternative impact scenarios have been proposed to improve results above the $\delta f_{\rm t} \approx -70\%$ of canonical models. High angular momentum impacts into rapidly spinning targets (Ćuk & Stewart 2012; Lock et al. 2018) can eject and mix more proto-Earth material, as can a very large impactor (Canup 2012). The excess angular momentum might be removable in or near the evection resonance, but removing the correct amount may be difficult (Rufu & Canup 2020). Hit-and-run impacts can also make somewhat more target-rich disks (Reufer et al. 2012). Multiple impacts could create successive intermediate satellites that combine to form the Moon (Rufu et al. 2017), depending on the merger efficiency (Citron et al. 2018a). Somewhat separately, a proto-Earth magma ocean could be more readily injected into orbit (Hosono et al. 2019), and numerical effects might be inhibiting mixing in simulations (Deng et al. 2019b). The circumstances required for some of these events may also have low likelihoods; however, with only one Moon to study, we are reminded that its origin could be improbable (Melosh 2014).

Numerical simulations of giant impacts commonly use smoothed particle hydrodynamics (SPH) to model planets using particles that evolve under gravity and pressure. Most previous Moon-formation simulations have used around 10^5–10^6 particles, but these resolutions can fail to converge on even large-scale outcomes of giant impacts, such as the planet's rotation period or the mass of ejected debris (Genda et al. 2015; Hosono et al. 2017; Kegerreis et al. 2019). Here we use up to 10^8 particles. At this resolution, each particle has a mass of 6×10^{16} kg and an effective size in the planet of ∼14 km. A lunar-mass satellite itself would be composed of around 10^6 particles, which enables us to inspect its composition in detail.

Directly produced satellites were found in some early simulations of giant impacts (Benz et al. 1987; Canup & Asphaug 2001) but have typically been dismissed in terms of

lunar formation (Canup & Asphaug 2001; Asphaug 2014) because of (1) then-justified low-resolution numerical concerns, (2) a lack of iron and of proto-Earth material, (3) overly fine-tuned requirements for the impact parameters, and/or (4) orbits that crossed interior to the Roche limit. In contrast, here with orders of magnitude more particles, we find that stable satellites are produced (1) reliably at high numerical resolutions of at least 10^7 SPH particles, (2) with a Moon-like mass of iron and significant proto-Earth material, and (3) over a small but appreciable range of impact angles and speeds especially for spinning planets (Ruiz-Bonilla et al. 2021), as well as that (4) satellites with Roche-interior initial trajectories often survive partial disruption to be torqued onto wider final orbits.

2. Methods

2.1. Initial Conditions

The proto-Earth target and Theia impactor are differentiated into an iron core and a rocky mantle containing 30% and 70% of the mass, respectively, with fiducial canonical-like masses of 0.877 and 0.133 $M_\oplus$. We use the updated ANEOS $Fe_{85}Si_{15}$ (Earth-core analog) and forsterite equations of state (EOSs; Stewart et al. 2019), which encompass thermodynamically consistent (no-tension) models of multiple phases and improved fits to experimental data. The default temperature at the surface is set to 2000 K, for a mantle specific entropy of 2.9 kJ K^{-1} kg^{-1}. The internal profiles are adiabatic with continuous temperature across the core–mantle boundary.

The planets' internal profiles are generated by integrating inward while maintaining hydrostatic equilibrium,[5] and then the roughly equal-mass particles are placed to precisely match the resulting density profiles using the stretched equal-area method[6] and its modified version for spinning planets (Ruiz-Bonilla et al. 2021). Before simulating the impact, a brief 10 ks settling simulation is first run for each body in isolation, to allow any final settling to occur. The specific entropies of the particles are kept fixed, enforcing that the particles relax themselves adiabatically.

2.2. Smoothed Particle Hydrodynamics Simulations

We run the ∼400 impact simulations in this study using the open-source hydrodynamics and gravity code SWIFT.[7] Most of these use a "vanilla" form of SPH plus the Balsara (1995) switch for the artificial viscosity (Kegerreis et al. 2019), to a simulation time of 90, 120, or 180 ks (25–50 hr) depending on whether, e.g., tidal stripping or secondary impact events have concluded, in a cubic box of side 120 $R_\oplus$. Any particles that leave the box are removed from the simulation.

To test the sensitivity of our results to the numerical methods and to known challenges for SPH, an additional set of comparison simulations are run using (1) the boundary-improvement methods of Ruiz-Bonilla et al. (2022), where a simple statistic is used to identify and then correct particles with inappropriate SPH densities near material interfaces and free surfaces, which mitigates the problems raised by density discontinuities in standard SPH; and (2) the geometric density average force (GDF) expression for the SPH equations of motion (Wadsley et al. 2017), which can further improve behavior near sharp density gradients.

2.3. Impact Scenarios and Simulation Suites

We start from a base scenario similar to a canonical Moon-forming impact: an impact angle of $\beta = 45°$; a speed at contact of the mutual escape speed, $v_c = 1\ v_{esc}$ (∼9 km s^{-1}); masses for the target proto-Earth and impactor Theia of $M_t = 0.887$ and $M_i = 0.133\ M_\oplus$; and no pre-impact spins (as illustrated in Appendix A, Figure A1).

The largest set of scenarios finely covers a focused range of angles and speeds: $\beta = 43°$, 44°, 45°, 46°, 47°, 48° and $v_c = (0.98, 1.00, 1.02, 1.04)v_{esc}$. This corresponds to angular momenta from 1.19 to 1.37 times that of the present-day Earth–Moon system, $L_{EM} = 3.5 \times 10^{34}$ kg m^2 s^{-1}. To examine the numerical effects of our finite-particle model planets, each scenario in this set is repeated 8 times using a rotated orientation for the settled target or impactor. For the other sets of simulations, rather than attempting a complete sampling of the many-dimensional parameter space, we explore a coarser range of more highly varied values, to test whether our conclusions are sensitive to significant changes of the body masses, spins, and temperatures.

We run a similar angle exploration for different-mass bodies, using $\frac{3}{4}$ and $\frac{1}{2}$ of the base Theia's mass and keeping the total mass constant: $M_i = 0.100$ and $0.067\ M_\oplus$, and corresponding $M_t = 0.920$ and $0.953\ M_\oplus$. For these smaller impactors, qualitatively similar outcomes arise at larger impact angles. As such, we test $\beta = 45°$–$50°$ for the $\frac{3}{4}$ mass Theia and $\beta = 52°$–$57°$ for the $\frac{1}{2}$ mass Theia, in 1° increments.

We then return to the base scenario and vary the pre-impact spin of each body, for spin angular momenta of $L_{t,i} = \left(-\frac{1}{2}, -\frac{1}{4}, \frac{1}{4}, \frac{1}{2}\right) L_{t,i}^{max}$, where L^{max} corresponds to the maximum stable spin (minimum period) for these planets (Ruiz-Bonilla et al. 2021): 1.0×10^{35} kg m^2 s^{-1} (2.3 hr) for the proto-Earth, and 4.9×10^{33} kg m^2 s^{-1} (2.5 hr) for Theia. The $\frac{1}{4}$ and $\frac{1}{2}$ L^{max} spin periods are 5.2 and 3.0 hr for the proto-Earth and 5.4 and 3.2 hr for Theia. The spinning bodies' axes of rotation are set in the same direction as the orbital angular momentum of the impact ($+z$), such that the impact point is on the equator and the spin is expected to have the greatest overall effect on the outcome. One additional proof-of-concept simulation with $10^{7.5}$ particles is run with the proto-Earth's spin angular momentum $\left(\sim\frac{1}{4} L_t^{max}\right)$ in the $+y$-direction, misaligned from the orbit such that Theia collides with primarily north-pole material.

We also test different temperature profiles for both planets, repeating the first set of angle and speed scenarios using surface temperatures of 1000 K, the base 2000 K, and 3000 K, yielding profiles below, slightly below, and above solidus, respectively. These lower and higher temperatures increase and decrease the bodies' average densities by about 3% and 7% for the proto-Earth and 4% and 10% for Theia, as well as testing the sensitivity to different regimes in the EOS.

Finally, we repeat a subset of the first suite of scenarios to study numerical reliability and convergence. The sets described above all use $\sim 10^7$ SPH particles, compared with the 10^5–10^6 typically used in the current literature, which can be insufficient

[5] The WOMA code (Ruiz-Bonilla et al. 2021) for producing spherical and spinning planetary profiles and initial conditions is publicly available with documentation and examples at https://github.com/srbonilla/WoMa and the Python module `woma` can be installed directly with pip.

[6] SEAGEN (Kegerreis et al. 2019) is publicly available at https://github.com/jkeger/seagen, or as part of WOMA.

[7] SWIFT (Schaller et al. 2018) is publicly available at www.swiftsim.com.

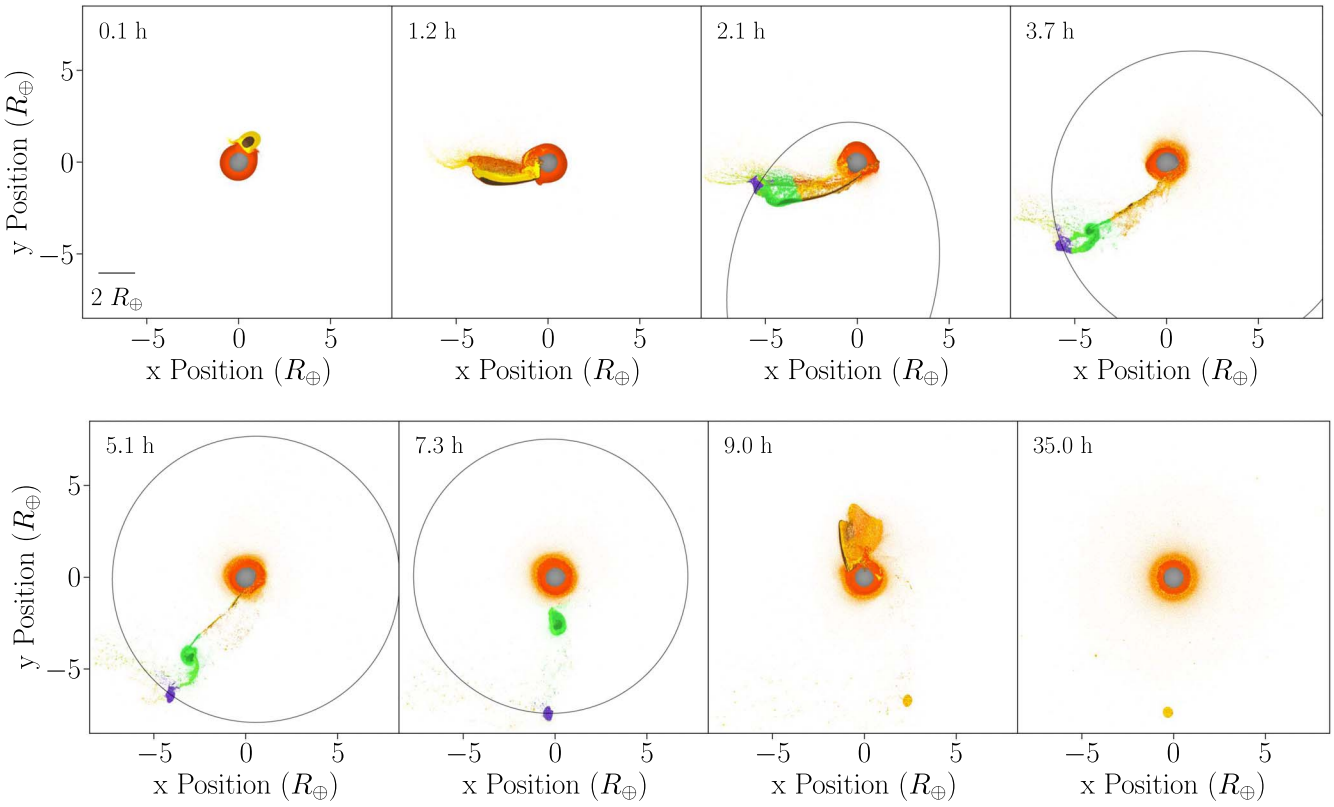

Figure 1. Illustrative snapshots from an impact simulation where a satellite is placed directly onto a wide orbit, in this example with the lowest final eccentricity. In the middle panels, the particles that will form the satellite and inner remnant are highlighted in purple and green. The black lines show the estimated orbit. Gray and orange show the proto-Earth's core and mantle material, respectively, and brown and yellow the same for Theia. The color luminosity varies slightly with the internal energy. The annotated time is measured from first contact, so the simulation began at −1 hr. An animation is available at http://icc.dur.ac.uk/giant_impacts/moon_wide_orbit_slice.mp4, and with the same data rendered in 3D at http://icc.dur.ac.uk/giant_impacts/moon_wide_orbit_houdini.mp4.

to resolve or converge on both small- and large-scale outcomes of giant impacts (Genda et al. 2015; Hosono et al. 2017; Kegerreis et al. 2019). We repeat the $\beta = 44°$–$47°$, $v_c = (1.00, 1.02)v_{esc}$ scenarios with 10^4, $10^{4.5}$, 10^5, $10^{5.5}$, 10^6, $10^{6.5}$, $10^{7.5}$, and 10^8 particles. The same scenarios are also repeated for 10^7 particles using the modified SPH scheme with the GDF (Wadsley et al. 2017) and boundary-improvement modifications (Ruiz-Bonilla et al. 2022). In addition, for the base scenario for each resolution below $10^{7.5}$ we also run eight reoriented repeats, as done for the full 10^7-particle angle and speed suite.

3. Results and Discussion

3.1. Immediate Satellite Formation

We find that a key feature of impact scenarios that launch a large satellite directly into a wide orbit is the early separation of the proto-satellite from the main remnant of the impactor. This behavior emerges reliably with sufficient numerical resolution. The inner remnant then transfers angular momentum to the satellite of ejected proto-Earth and Theia material and slingshots it into orbit, as illustrated in Figure 1, before falling back to re-impact the target.

The initial satellite separation is consistent for simulations with over $10^{6.5}$ SPH particles, up to and including our highest resolution of 10^8, as shown in Figure 2. A full investigation of what determines the exact number of particles required to resolve adequately the tidal and hydrodynamic evolution at this scale is left for future work. Lower resolutions instead produce a single larger remnant that stays intact until it grazes or re-impacts the proto-Earth to produce a spray of debris.

In the particular scenario of Figure 1, the satellite actually overtakes the inner remnant briefly around 5 hr (fifth panel), and the now-reversed torque slightly shrinks and circularizes the final orbit. This resulting satellite has a mass of 0.69 $M_\mathbb{C}$ and a nearly circular orbit with a periapsis of 7.1 $R_\oplus$, far outside the Roche limit of ∼2.9 $R_\oplus$ and even likely beyond the evection and eviction resonances for a moderate rotation period (Touma & Wisdom 1998; Ćuk & Stewart 2012). The observed transfer of angular momentum is also matched well by simple estimates for the forces between the orbiting bodies (Appendix A, Figure A2).

This direct formation of a satellite is sensitive to the impact angle, with milder dependencies on the speed and initial spins, as detailed further in Appendix B. Large satellites are best produced at impact angles around 45°—the most likely angle for a generic impact—and near the mutual escape speed. For nonspinning planets, the range of satellite-producing impact angles is only a few degrees, but for spinning planets, wider ranges become feasible. In particular, a prograde-spinning proto-Earth allows less disruption of Theia for viable satellite formation at lower angles, although high initial rotation rates may require some angular momentum to be removed from the final system (Rufu & Canup 2020).

The initial temperature and internal structure of the proto-Earth and Theia do not substantially affect these results. Even a much smaller Theia with $\frac{3}{4}$ the mass still produces similar stable satellites, at larger impact angles. Similar outcomes were

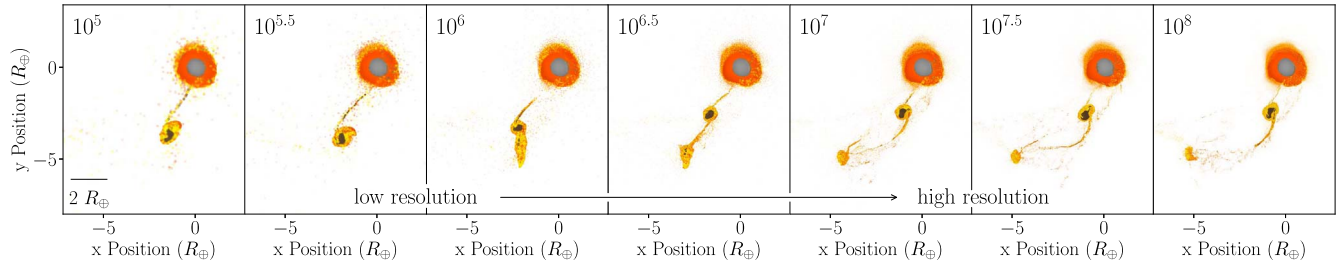

Figure 2. The categorically distinct behavior of outer-satellite formation emerges consistently for resolutions above a threshold of $>10^{6.5}$ particles. Each panel shows a snapshot from simulations of the same scenario at the same time 3.6 hr after impact using different numbers of particles. 10^4 and $10^{4.5}$ particles (not shown) behave similarly to 10^5.

also found using different EOSs (Ruiz-Bonilla et al. 2021) and using a modified version of SPH that mitigates known issues at boundaries between materials and vacuum surfaces (Ruiz-Bonilla et al. 2022). The region of parameter space for the immediate formation of stable satellites is not huge but appears to be numerically robust and not restricted to any low-likelihood parameter values.

3.2. Tidal Stripping onto Stable Orbits

In some scenarios, the satellite is not launched out quite as far, and its periapsis falls within the Roche limit. However, not only can these satellites survive partial tidal disruption on their initial orbit, but the stripped material can also transfer angular momentum to the surviving satellite and torque it onto a stable, Roche-exterior final orbit. This significantly extends the parameter-space range of scenarios that produce a Moon-like satellite.

The change in mass, periapsis, and eccentricity from all large satellites that pass near or inside the Roche limit and survive with at least 10% of their initial mass is shown in Figure 3. Depending on their initial orbits, satellites may lose little to no mass; lose some mass and be torqued onto stable orbits, from initial periapses as low as $\sim 2.4\,R_\oplus$; or suffer near-total disruption and be ejected onto unbound orbits. The estimated Roche limit of $2.9\,R_\oplus$, which assumes a circular orbit, is a decent prediction for the farthest distance at which these satellites on eccentric orbits begin to be partially disrupted.

In most cases, the partial stripping and resulting transfer of angular momentum mildly increase the eccentricity of the final satellite. However, a significant minority have their eccentricity reduced, usually when the stripping occurs late enough that a torque is still applied as the satellite approaches apoapsis. Regardless, the periapsis distance is raised in every case of significant mass loss, often to well beyond the Roche limit.

This general behavior is remarkably consistent given the diversity in mass, initial orbit, spin, and debris environment of the pre-periapsis satellites, with a dominant dependency on the initial periapsis, r_p. We find that the fraction of mass that survives passage inside the Roche limit, $m_\mathrm{f}/m_\mathrm{i}$, is fit well by a simple analytical prediction (Figure A7), derived in Appendix A.2:

$$\frac{m_\mathrm{f}}{m_\mathrm{i}} \approx \frac{r_\mathrm{p}^3}{t_\mathrm{Roche}} \sqrt{\frac{2\pi\rho}{3GM^2}}, \tag{1}$$

where t_Roche is the time spent within the Roche limit as predicted from the initial orbit, ρ the satellite's density, and M the planet's mass.

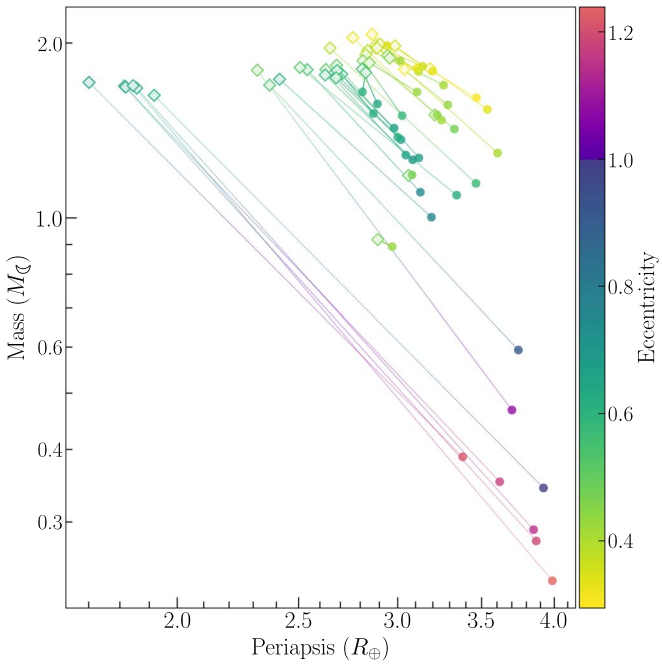

Figure 3. The change in mass, periapsis, and orbital eccentricity of satellites that pass through a periapsis near or inside the Roche limit and retain at least 10% of their initial mass, which tends to result in a significantly wider final orbit following partial tidal stripping. Diamonds and circles show the pre- and post-periapsis satellites, respectively.

Across the tested impact scenarios, the major outcomes and conclusions for forming stable satellites are consistent for simulations with $\geqslant 10^7$ particles. However, these multistage collisions and stripping events are somewhat chaotic; small changes to the initial satellite can have larger consequences for its evolution. We probe this uncertainty by running additional simulations of the same scenario with reoriented initial conditions, which with infinite resolution should give identical outcomes. Higher resolutions do reduce the scatter in results, but the precise values for the masses and orbits of the final satellites are not yet perfectly converged, as shown in Figure 4. At standard/low resolutions below $10^{6.5}$ particles, the formation of the initial satellite is not resolved reliably, so instead a wider variety of low-mass final bodies are formed. At higher resolutions, some initially similar satellites may dip within the Roche limit briefly enough to suffer minimal tidal stripping, while others with just slightly lower periapses can have enough material removed to be torqued onto somewhat wider orbits (Figure A5).

The longer-term evolution of these satellites will largely depend on the tidal interactions and angular momentum

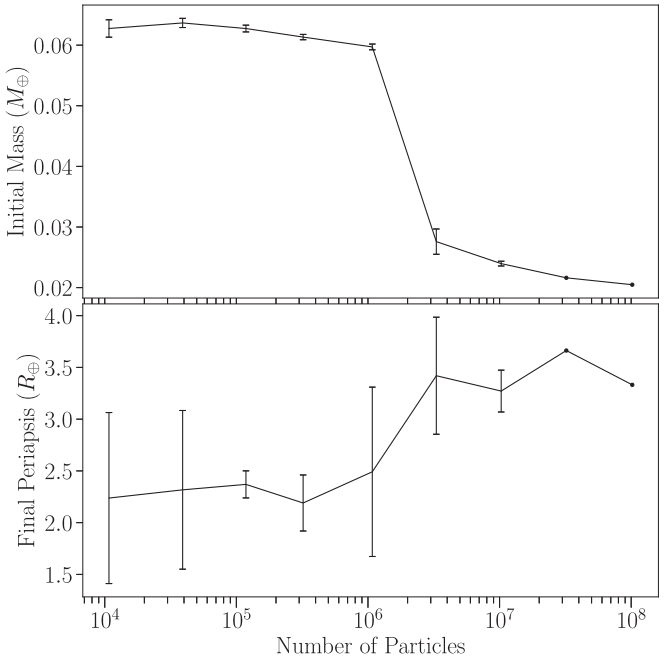

Figure 4. The convergence and uncertainty of the mass of the initial satellite (or larger single remnant) and the periapsis of the final satellite that form in different-resolution simulations of the impact scenario in Figure 2, as a function of the number of particles. The error bars show the standard deviations across eight reoriented repeats, with points for the individual $10^{7.5}$- and 10^8-particle simulations.

transfer from the rapidly spinning Earth and the disk (Goldreich & Tremaine 1980; Touma & Wisdom 1994), and perhaps on friction with extended disks on shorter timescales. Additionally, larger disks might produce other moonlets (Rufu et al. 2017; Citron et al. 2018b), and satellites may accrete significant additional material from the debris disk (Salmon & Canup 2012; Lock et al. 2018).

3.3. Satellite Compositions and Interiors

Canonical Moon-forming scenarios produce debris disks composed of only ∼30% proto-Earth material (Canup et al. 2021), which is difficult to reconcile with the near-identical isotopic signatures of Earth and the Moon. Here, the immediate satellites typically have moderately higher bulk compositions of around 30%–40% proto-Earth material. Furthermore, most show a strong gradient in provenance with radius, with a deep interior of mostly Theia material under a roughly linearly increasing and isotropic proportion of proto-Earth mantle (Ruiz-Bonilla et al. 2021). The remaining debris disks (see Table 1), from which a satellite may later accrete more mass, contain similar amounts of proto-Earth and Theia material.

In otherwise Moon-like satellites, the outer ∼10% by radius can reach over 60% proto-Earth material. The outer 30% by radius ($\sim\frac{2}{3}$ the mass) then averages to around 40%–50% proto-Earth. This corresponds to a depth of about 500 km, relatable to the ∼300–1000 km depths that are considered for the lunar magma ocean (Charlier et al. 2018; Johnson et al. 2021), within which an initial gradient may be expected to mix.

The outer material is molten, typically heated to at least 4000 K by the impact, but the deeper interior is only a few hundred kelvin above its initial near-solidus state, in contrast with the fully molten satellites expected to accrete from most debris disks (Pritchard & Stevenson 2000; Lock et al. 2020). Our cooler, default, and warmer planet initial conditions thus produce satellites with mostly solid, sub-liquidus melt, and molten interiors, respectively.

The deep interiors of all our simulated satellites contain some iron from the impactor's core. For satellites with masses similar to the Moon, the typical iron content ranges from around 0.1% to 3%, comparable with the ∼1% mass of the lunar core (Williams et al. 2014).

3.4. Satellite Inclination from Misaligned Target Spin

Previous Moon-formation scenarios yield debris disks that are closely aligned with Earth's equator. This conflicts with the initial orbital tilt away from the equator of 10° or higher that could explain the Moon's present-day ∼5° inclination (Touma & Wisdom 1998; Ćuk et al. 2016). This issue has prompted alternative suggestions involving resonances with debris or the Sun (Ward & Canup 2000; Tian & Wisdom 2020), or close encounters with planetesimals (Pahlevan & Morbidelli 2015).

In contrast, we find that an impact onto a spinning target with angular momentum misaligned to that of Theia's orbit can readily produce significantly inclined debris including a satellite, as illustrated in Figure 5. In this example, the satellite is created similarly to the equatorial cases described above, with a mass of 1.4 $M_\mathbb{C}$, a periapsis of 3.1 $R_\oplus$, and an inclination of 32°.

4. Implications and Conclusions

To determine whether these satellites can explain other properties of the Moon in addition to the mass and iron content, such as those without fully molten interiors, bespoke future studies are required to extrapolate the simulation outputs reliably to the present day—as remains an ongoing challenge for standard debris-accretion models as well (Lock et al. 2020; Canup et al. 2021). With this in mind, here we briefly speculate on the possible implications and distinctions from other scenarios.

If the gradient of proto-Earth material in the satellite is entirely mixed away, then we would find $\delta f_t \approx -60\%$, only slightly better than canonical models. However, if it does survive even partially, depending on some imperfect extent of radial mixing that may be helped by the cooler interior, then this improves δf_t to around −40% to −30%, similar to proposed hit-and-run scenarios (Reufer et al. 2012). If the outer ∼0.15 $R_\oplus$ of Earth's mantle also remains distinct, which could help to explain geochemical heterogeneities (Nakajima & Stevenson 2015; Deng et al. 2019a), then our δf_t would increase by an additional ∼10%. A "hit-and-run-return" collision can both give a higher likelihood for a canonical-speed final impact like those considered here and raise δf_t by another ∼10% (Asphaug et al. 2021), yielding $\delta f_t \approx -20\%$ to −10% for these immediate satellites. Magma oceans on the proto-Earth may raise this even further (Hosono et al. 2019). This result could resolve the isotopic conundrum for a range of Theia compositions even if only a subset of these processes are effective (Meier et al. 2014; Asphaug et al. 2021), but it warrants in-depth study of the long-term thermal and tidal evolution.

These directly formed satellites also provide a hitherto-overlooked range of initial conditions for the Moon's early evolution: with a wider and/or more eccentric or inclined orbit —outside the Roche radius and potentially also the evection and eviction resonances—and the option of a solid or partial-melt interior. For example, the Moon's thin crust may not be

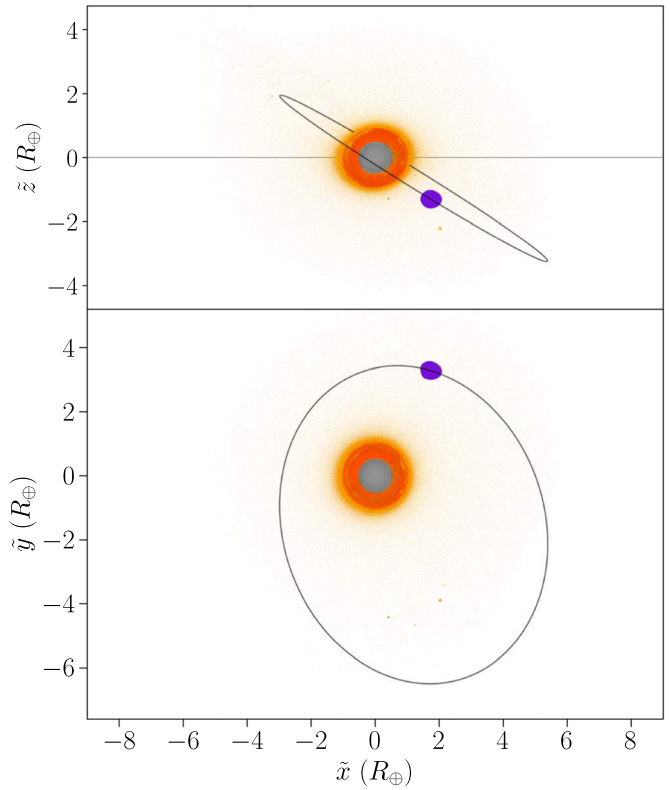

Figure 5. The inclined satellite produced by an impact onto a spinning proto-Earth misaligned to Theia's orbital angular momentum, shown as in Figure 1. The $\tilde{z}$-direction is set as the orientation of the post-impact planet's spin angular momentum, which is estimated simply as the total over all particles within $2\,R_\oplus$. The results are not sensitive to this choice, as using $1.5\,R_\oplus$ or $2.5\,R_\oplus$ only changes the inferred satellite inclination by $<0.5°$.

consistent with the fully molten Moon expected from the accretion of hot debris in other models (Pritchard & Stevenson 2000; Charlier et al. 2018; Johnson et al. 2021). A cohesive interior and noncircular orbit might also help to explain the lunar fossil figure, depending on the extent of tidal heating (Matsuyama et al. 2021). In addition, the compositional gradient aligns with measurements of less Earth-like isotopes in the deep lunar mantle (Cano & Sharp 2020). The lunar volatile signature may be difficult to reproduce without a prolonged disk phase (Dauphas et al. 2022), but loss from a magma ocean might be sufficient (Day et al. 2020), and significant disk material could also be later accreted onto the satellite's sampled exterior (Salmon & Canup 2012; Citron et al. 2018b). Finally, a satellite on a wide, significantly inclined orbit, which we demonstrate can be produced by a misaligned pre-impact spin, could preserve its inclination to help to explain the Moon's tilted orbit (Ćuk et al. 2016; Tian & Wisdom 2020).

In conclusion, high-resolution simulations reveal how giant impacts can immediately place a satellite into a wide orbit with a Moon-like mass and iron content. The resulting outer layers rich in proto-Earth material and the new options opened up for the initial lunar orbit and internal structure could help to explain the isotopic composition of the Moon and other unsolved or debated lunar mysteries. The system's angular momentum can range from the present-day to higher values, especially as the spin of the proto-Earth is increased. Satellites that pass inside the Roche limit can predictably survive on new, higher-periapsis orbits. This extends the range of scenarios that can produce Moon-like satellites and is a relevant process to consider in other planetary systems. The likelihood and potential of this and other Moon-formation scenarios will be constrained by: more reliable models for the long-term evolution of satellite orbits, magma oceans, post-impact planets, and disks; further improved EOSs in high-resolution simulations across more of the wide parameter space; and deeper understanding of the isotopic and other constraints from existing and future measurements (Lock et al. 2020; Canup et al. 2021).

This work was supported by a DiRAC Director's Discretionary Time award, by Science and Technology Facilities Council (STFC) grants ST/P000541/1 and ST/T000244/1, and used the DiRAC@Durham facility managed by the Institute for Computational Cosmology on behalf of the STFC DiRAC HPC Facility (www.dirac.ac.uk). This equipment was funded by BEIS via STFC capital grants ST/K00042X/1, ST/P002293/1, ST/R002371/1, and ST/S002502/1, Durham University, and STFC operations grant ST/R000832/1. DiRAC is part of the National e-Infrastructure. We also thank Kevin Zahnle for comments. The research in this paper made use of the SWIFT open-source simulation code (Schaller et al. 2018), version 0.9.0. J.A.K. acknowledges support from STFC grants ST/N001494/1 and ST/T002565/1 and a NASA Postdoctoral Program Fellowship. S.R.-B. is supported by STFC grant ST/P006744/1 and Durham University. V.R.E. and R.J.M. are supported by STFC grant ST/T000244/1. T.D. S. is supported by STFC grants ST/T506047/1 and ST/V506643/1. L.F.A.T. acknowledges support from NASA Emerging Worlds Program award 80NSSC18K0499.

Software: SWIFT (www.swiftsim.com, Schaller et al. 2018, version 0.9.0); WOMA (pypi.org/project/woma/, Ruiz-Bonilla et al. 2021).

Appendix A

Figure A1 shows a diagram of the impact initial conditions.

Torques and Tidal Stripping

The main text describes how a satellite on a wide orbit is produced in scenarios like the one illustrated by Figure 1. The orbital evolution of the interacting outer satellite and inner remnant in that example are shown in Figure A2. To estimate the evolution of the satellite's orbital angular momentum, we integrate the acceleration from the tangential component of the force from the inner remnant, i.e., the force perpendicular to the radial vector to the planet. The predicted increase of the satellite's orbital angular momentum matches the simulation fairly well (dashed line in Figure A2). This estimate uses the centers of mass taken from the already-run simulation, so the agreement is more of an encouraging confirmation that the torque explains the evolution than a predictive model for generic scenarios.

The satellite and inner-remnant particles are selected using a standard friends-of-friends (FoF) algorithm with a linking length of $0.017\,R_\oplus$. The selected masses and results are not affected by small changes to this value. For final satellites, we require a minimum of 50 particles to form an FoF group.

A.2. Tidal Stripping onto a Stable Orbit

If the torque from the inner remnant is not quite enough to raise the satellite's orbit outside the Roche limit of $\sim 2.9\,R_\oplus$, then as it passes through periapsis it will be tidally disrupted, to

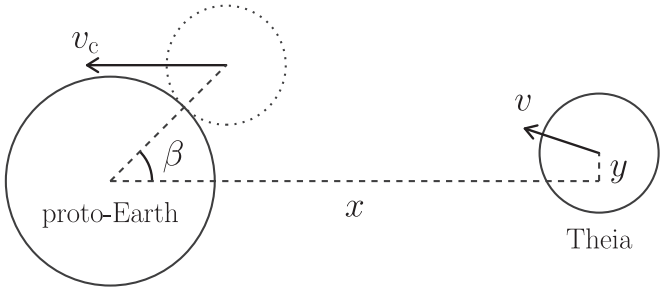

Figure A1. The initial conditions for an impact scenario, to scale, in the proto-Earth target's rest frame. The angle and speed at first contact, β and v_c, are set neglecting any tidal distortion before the collision. The initial separation is set such that the time to impact is 1 hr, as detailed in Kegerreis et al. (2020, Appendix A), with the velocity at contact in the $-x$-direction.

some extent. However, the stripped material can exchange angular momentum with the surviving body and torque it again onto a more stable orbit, as illustrated in Figure A3. In this example, the initial satellite falls deep inside the Roche limit with a periapsis of 2.6 $R_\oplus$. It loses about one-third of its mass, stripped out into a long tidal tail, for a final mass of 1.1 $M_\mathbb{C}$. The surviving satellite continues on a new orbit with its periapsis raised outside the Roche limit to 3.1 $R_\oplus$, protecting it from further disruption.

As with the previous example, we can examine this evolution using the centers of mass of the two pieces, shown in Figure A4. Here the predicted angular momentum evolution is still a helpful sanity check but matches the simulation a bit less precisely, perhaps because a point mass is a worse approximation for the elongated tail of stripped material than a more condensed inner remnant.

This type of tidal stripping process exacerbates the differences in the detailed outcomes between reoriented repeat simulations, as discussed with respect to Figure 4 in the main text. The orbits of satellites before and after periapsis from the same scenario are shown in Figure A5, illustrating how similar initial satellites can separate into a wider spread of final results —although the primary conclusions for the creation of a large stable satellite remain consistent.

A.3. Tidal Stripping Trends and Predictions

As mentioned in the main text, we find a wide variety of satellites that suffer different amounts of tidal disruption by falling within the Roche limit and may be torqued onto wider orbits (see Figure 3). These pre-periapsis satellites produced naturally from the initial impacts do not evenly tile the parameter space, but they cover enough of a range for us to examine the general behavior and trends and to derive and test a simple model for the fraction of lost mass.

Note also that this empirical set includes scenarios with, for example, significantly different-size and different-composition bodies, other debris also in orbit, and rapidly spinning initial satellites, all of which likely add noise to these results. A more thorough and systematic exploration is left for future work.

At a distance d from the planet, at a point r from the center of the satellite (see the diagrams in Figure A6), the tidal acceleration is $GM2r/d^3$. Crudely approximating this acceleration as constant for the time the satellite spends inside the Roche limit, $t_{\rm Roche}$, and setting the distance equal to the periapsis to calculate the maximum acceleration, $d = r_{\rm p}$, we assume that the material will be removed if it is accelerated to the escape speed of the satellite, $\sqrt{2Gm_{\rm i}/R}$, where $m_{\rm i}$ and R are

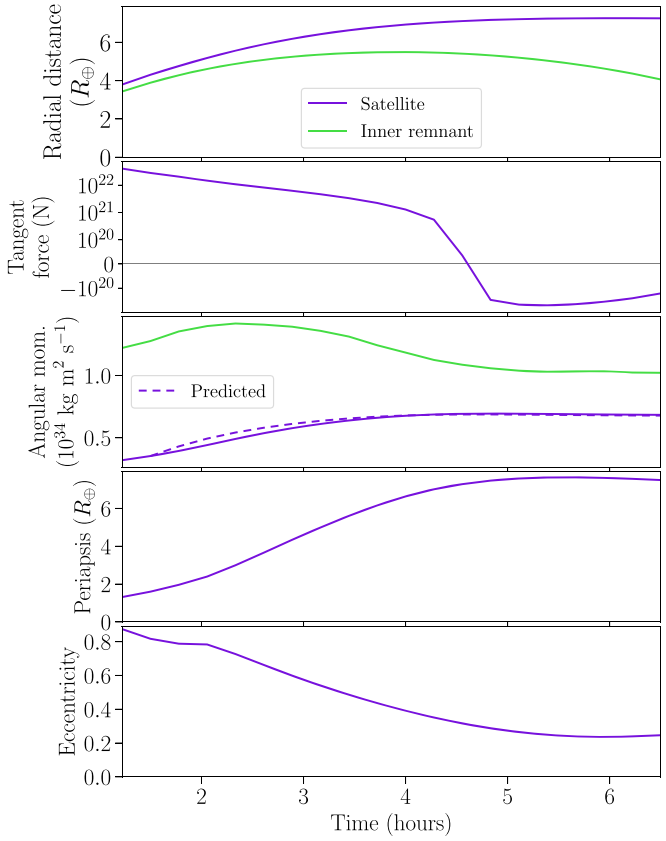

Figure A2. The early orbital evolution of the forming satellite and inner remnant highlighted in matching colors in Figure 1. The panels show the radial distances of the bodies from the central planet, the tangential component of the force from the inner body on the satellite, the change in each body's angular momentum and the prediction for that of the satellite from the tangential force (dashed line), the satellite's periapsis, and its eccentricity.

its initial mass and radius. We further approximate the final mass as proportional to the radius beyond which material is lost, $m_{\rm f}/m_{\rm i} \approx r/R$, equivalent to treating the satellite as a cylinder that is cleanly split. This yields

$$\frac{m_{\rm f}}{m_{\rm i}} \approx \frac{r_{\rm p}^3}{t_{Roche}} \sqrt{\frac{2\pi\rho}{3GM^2}}. \tag{A1}$$

The time spent inside the Roche limit can be estimated using the area of the shaded region in the bottom panel of Figure A6. By the general property of ellipses, this is b/a of the lightly shaded region bounded by the auxiliary circle, where b is the semiminor axis. That lightly shaded area is the sector with area $\frac{1}{2}a^2E$ minus the triangle of base ea with area $\frac{1}{2}ea^2\sin(E)$:

$$\begin{aligned}
\phi &= \cos^{-1}\left[\frac{1}{e}\left(1 - \frac{a(1-e^2)}{R_{Roche}}\right)\right] \\
E &= 2\tan^{-1}\left[\sqrt{\frac{1-e}{1+e}}\tan\left(\frac{\pi-\phi}{2}\right)\right] \\
t_{Roche} &= \frac{\frac{1}{2}ab(E - e\sin(E))}{\frac{1}{2}\pi ab}\, t \\
&= \frac{E - e\sin(E)}{\pi}\, t,
\end{aligned} \tag{A2}$$

where T is the orbit period.

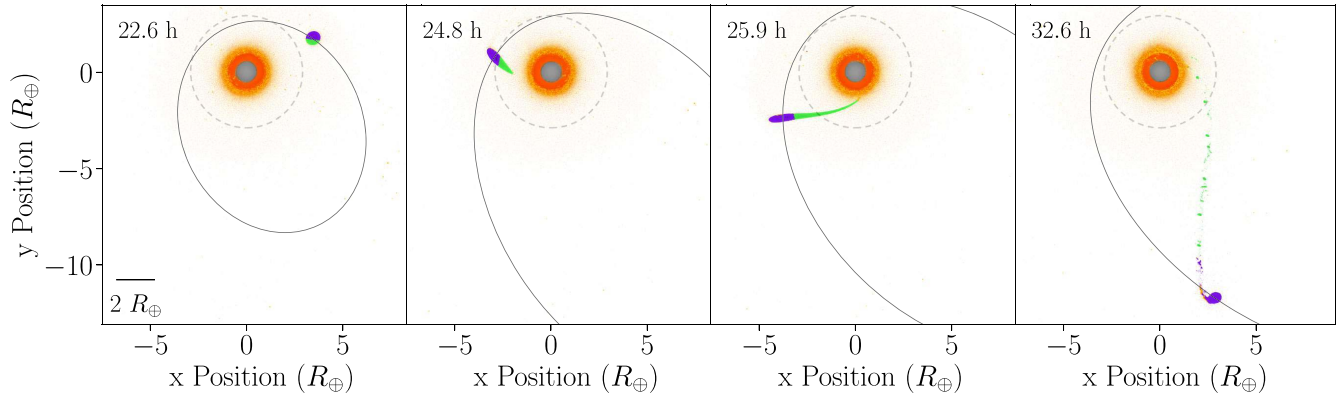

Figure A3. Illustrative snapshots of the first periapsis passage after the satellite-forming initial impact, from a simulation where the final satellite ends up on a stable orbit. Colors and annotations are the same as in Figure 1, except here purple and green highlight the material that will end up in the final satellite and that will be stripped from the initial body, respectively. The dashed line indicates the Roche limit. An animation is available at http://icc.dur.ac.uk/giant_impacts/moon_strip_orbit_slice.mp4, and with the same data rendered in 3D at http://icc.dur.ac.uk/giant_impacts/moon_strip_orbit_houdini.mp4.

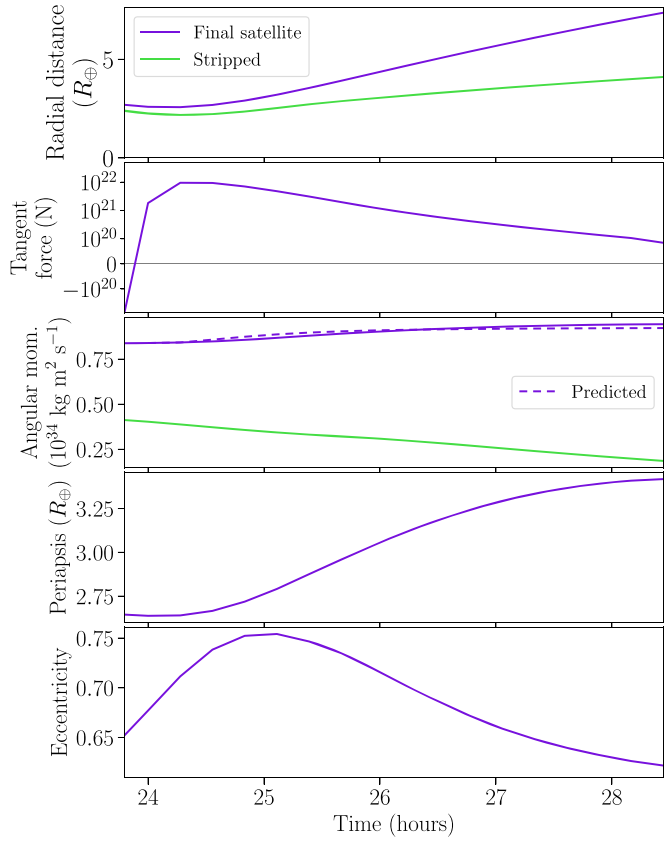

Figure A4. The orbital evolution of the material that survived and that was stripped from the initial satellite in the periapsis passage illustrated in Figure A3, presented as in Figure A2.

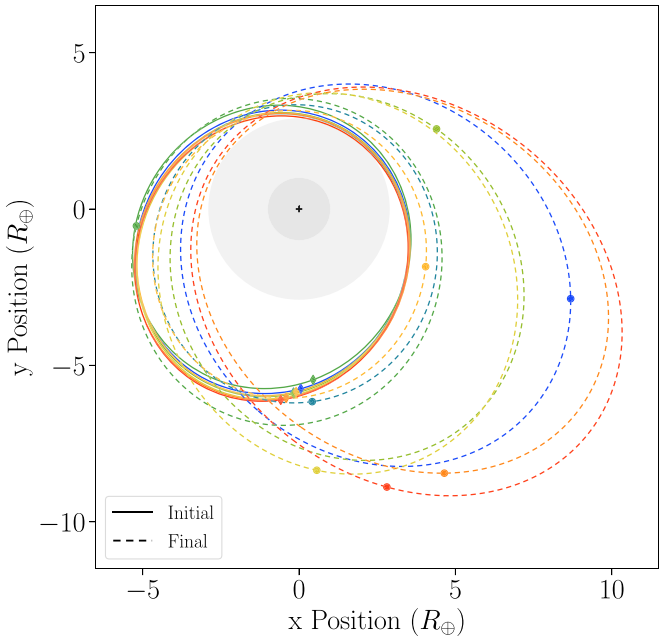

Figure A5. The positions and orbits of the satellites produced by eight reoriented repeats of the same scenario as in Figures 2 and 4 with 10^7 particles, at the same times before (solid lines and diamonds) and after (dashed lines and circles) the first periapsis tidal-stripping event. The inner and outer gray circles indicate the planet's radius and the Roche limit at about 1 and 2.9 $R_\oplus$, respectively.

The mass fractions that survive stripping from the simulations are shown in Figure A7 (see also Figure 3). The overall trend matches the predicted scaling of the final mass with the cube of the initial periapsis. Furthermore, given the simplicity of the model assumptions compared with the dynamic complexity of the full simulated events, the individual estimates for each initial satellite agree remarkably well in most cases.

The vertical scatter away from the power-law trend correlates mildly with the spin, shown by the color in Figure A7. This hints at an intuitive link whereby rapidly rotating and more oblate satellites lose mass more readily. However, given that the effect is relatively minor, confirming this would warrant a study in which the parameters are systematically varied in isolation, since many of the different-spin cases seen here also have different masses and other potentially degenerate properties.

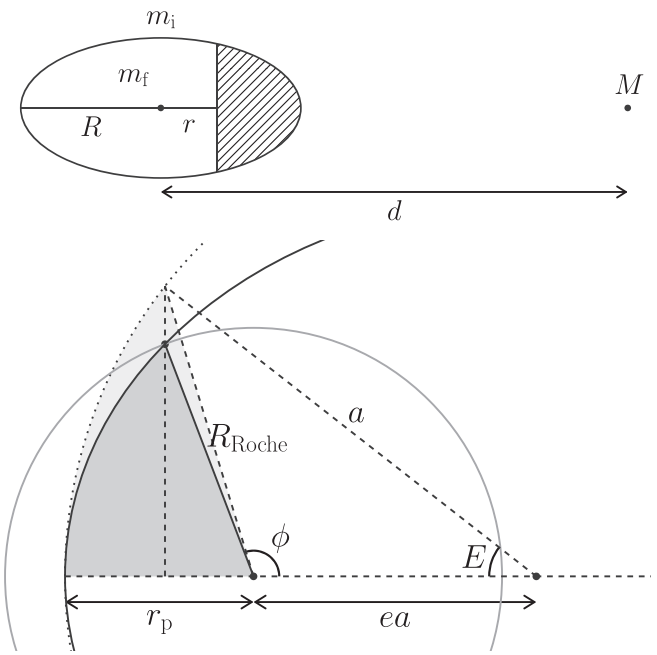

Figure A6. Diagrams for estimating the stripping of material when a satellite passes through periapsis within the Roche limit. Top: notation for the mass lost (hatched region) from the tidal force at a distance r from the center of a satellite with radius R and initial mass m_i, at a distance d from a planet with mass M. Bottom: notation for the time spent inside the Roche limit, R_{Roche} (gray circle), by a satellite on an orbit (black ellipse) with a semimajor axis a, eccentricity e, and periapsis $r_p < R_{Roche}$. ϕ is the complement to the true anomaly, and E is the eccentric anomaly. The dotted line shows the auxiliary circle.

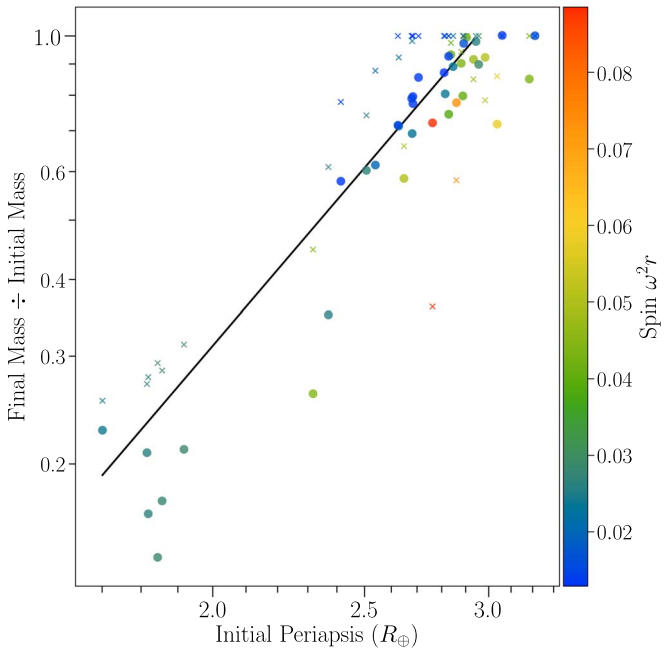

Figure A7. The fractional change in mass of satellites that are partially stripped through periapsis. The black line is the predicted power law of $m_f/m_i \propto r_p^3$, scaled in magnitude to fit the slow-spinning initial satellites. The crosses show the model predictions for each simulation using Equations (1) and (A2).

Appendix B
Exploring Parameter Space

Here we discuss the effects of changing different scenario parameters in a little more detail than in the main text. We start with the finely sampled set of impact angles and speeds and then explore the sets of coarser, more dramatic changes to the initial spins of each planet, their masses, and their temperatures, as detailed in Section 2.

B.1. Changing Angle and Speed

At lower impact angles (see Figure A1) than the examples described above, Theia is more disrupted as it collides deeper into the proto-Earth and is kept closer in. Plenty of material is still ejected to form an outer satellite, but the inner remnant is too distant from the satellite to torque it onto a sufficiently wide orbit. The outer body may then re-impact the planet following the inner one, resulting in a relatively smooth disk of debris, or will graze past it and be heavily tidally disrupted into a long chain of small, mostly unbound bodies.

At higher impact angles, Theia plows through the smaller mass of the proto-Earth that it encounters with less disruption. An outer satellite starts to form, but it remains too close to the inner one to stay separate, and they recombine before falling back to the planet. This large single body can be on a wide enough orbit that it barely recollides with the proto-Earth. In some cases that second impact can itself produce a variety of satellites in a similar manner to other scenarios, including on stable orbits, but usually with quite small masses.

Changing the impact speed has a less dramatic effect. As the speed increases, for all angles, the overall behavior is similar, with both the inner remnant and outer satellite forming farther from the proto-Earth and from each other. This extra separation can weaken the torque between them, but it conversely allows significantly more time for interaction, so it tends to place the satellites on closer to stable orbits. The general result for faster impacts is thus that similar-mass satellites form with mildly different trajectories. Large inner remnants that would re-impact the proto-Earth may instead pass by on a near miss and be dispersed into many small bodies in a large tidal tail. Outer satellites that would be highly disrupted by tides may reach a survivable or even Roche-exterior orbit.

At significantly higher speeds, the sprayed ejecta become unbound and/or too dispersed to form cohesive bodies, and the Theia remnant itself eventually escapes as a hit-and-run. There is a middle ground where a mostly intact impactor remains bound on a large orbit to return later, which effectively becomes a new impact of its own with much the same range of possible outcomes (Asphaug et al. 2021).

B.2. Changing Pre-impact Spin

The pre-impact rotation of both the target and impactor can have a significant effect on the outcome of giant impacts in general (Canup 2008; Asphaug et al. 2021; Ruiz-Bonilla et al. 2021), especially for the relatively rapid spins in these simulations. Regardless, we find that spinning bodies still produce stable immediate satellites in similar ways, and furthermore open up wider regions of the parameter space

than nonrotating ones. We denote spins with a positive angular momentum vector in the same direction as the orbital angular momentum as *prograde*, and opposite, negative ones as *retrograde*.

For a prograde proto-Earth and a given impact angle, the overall behavior is similar to a higher-angle nonspinning scenario. Theia collides with mantle material that is moving in the same direction, and so is less disrupted, and a satellite forms slightly later on in time. For both the $+0.25$ and $+0.5$ $L^{\rm max}$ targets, all tested angles $\leqslant 45°$ and $\leqslant 46°$, respectively, produce bound satellites outside the Roche limit. The total angular momentum is increased above the canonical $\sim 1.2\, L_{\rm EM}$ to ~ 2.7 and ~ 1.9, respectively, comparable to other high angular momentum impact scenarios (Canup 2012; Ćuk & Stewart 2012; Lock et al. 2018), though any intermediate values should also be viable in this case.

Conversely, a retrograde proto-Earth greatly disrupts the impactor into a spray of debris. This can collect into one or two clumps, but these tend to be too separated to fall into wide enough orbits as easily. Some scenarios do still produce satellites on stable but eccentric orbits. Furthermore, the total angular momentum is around half the present-day value, so a rapidly retrograde-spinning proto-Earth is not a viable scenario.

A prograde Theia can somewhat "roll" over the proto-Earth, but otherwise the behavior is similar to the nonspinning cases as the angle changes. As this spin increases further, the outer satellite tends to be ejected unbound. Theia's small mass means that even a rapid spin has only a small contribution to the total angular momentum.

A retrograde Theia sticks closer to the proto-Earth after the initial impact but can also be disrupted enough for a separate outer body to form successfully. For $L = -0.25\, L^{\rm max}$, the torque from the nearby inner remnant is strong enough to produce a stable satellite across a wider range of angles than the nonspinning case.

We did not explore the great variety of other options for the initial spins, most notably having both planets spin or allowing spin angular momenta not parallel to the orbital angular momentum beyond the proof-of-concept example shown in Figure 5. For now, we simply conclude that pre-impact spin has a fairly significant effect and can increase the viable region of parameter space for the immediate formation of stable satellites.

B.3. Changing Impactor Mass

For a fixed impact angle and speed, reducing Theia's mass so significantly relative to the proto-Earth produces very different outcomes. However, at larger impact angles, much of the same fiducial-mass behavior is then reproduced. The range of ideal satellite-producing angles is slightly narrower, but for the $\frac{3}{4}$ mass Theia we find the same trends for the formation of separate inner and outer bodies as the impact angle and speed change, including the placement of large satellites onto stable orbits well beyond the Roche limit. At these higher angles, the satellite and inner remnant tend to form further from the proto-Earth and from each other and so end up on more eccentric initial orbits.

The $\frac{1}{2}$ mass Theia also shows similar qualitative trends, at correspondingly even higher angles. However, the outer body then forms too far behind the inner remnant and is torqued onto an eccentric orbit without the periapsis being raised outside the Roche limit. It might be that a narrower range of angles and speeds exists where a stable satellite is produced, but at best the likelihood decreases somewhat for an impactor with a mass significantly lower than the canonical Theia's by more than a few tens of percent.

B.4. Changing Temperature

We probe the sensitivity to the internal structure of the two planets by significantly lowering and raising the surface temperatures of both planets, here by ± 1000 K. This corresponds to increasing and decreasing their densities by about 10% and 4%, respectively. Given the uncertainty in this aspect of the initial conditions, it is encouraging that the lower-temperature (higher-temperature) simulations generally show similar outcomes, with a mild trend of the inner remnants staying closer to (farther from) the planet. This is as might be expected from the relative ease with which warmer and lower-density planets can push through the initial impact. This results in the higher-temperature satellites being torqued slightly more readily onto wider orbits.

All of these simulations use the same ANEOS materials. However, similar satellite-forming results were found with previous simulations using the simpler Tillotson (1962) EOS and an even lower surface temperature of 500 K (Ruiz-Bonilla et al. 2021), further suggesting that our conclusions are not highly sensitive to the composition and density or thermal profiles of the planets.

Appendix C
Data Tables

Table 1 lists the primary results from all simulations, arranged in groups by subset, angle, and speed. Full simulation data will be shared on reasonable request. Note that the satellite values refer to only the single most massive body, if any; some scenarios also produce smaller satellites on stable orbits, especially if the largest one tabulated here is escaping unbound. Note also that the qualitative evolution of some scenarios has not progressed as far as others. For example, if the initial impactor remnant is set on an orbit with a period greater than 50 hr, then it will not yet have re-impacted the target. Similarly, long-period satellites may be headed toward significant future stripping events at periapsis.

Table 1
Results from the Simulations

Column	Parameter	Units	Description
1	Type		Changed parameters from the base scenario[a]
2	β	deg	Impact angle
3	v_c	v_{esc}	Speed at contact
4	m	$M_{\mathbb{C}}$	Mass of the largest satellite
5	r_p	$R_{\oplus}$	Periapsis of the largest satellite
6	e		Orbital eccentricity of the largest satellite
7	f_c	%	Mass fraction of core iron material of the largest satellite
8	$m_d^{a_{eq}}$	$M_{\mathbb{C}}$	Mass of the debris disk using the equivalent circular radius criterion
9	$m_d^{r_p}$	$M_{\mathbb{C}}$	Mass of the debris disk using the periapsis criterion
10	L_{bnd}	L_{EM}	Total angular momentum of all bound material
11	f_t^s	%	Mass fraction of target proto-Earth mantle (f_t) of the full satellite
12	$f_t^{s,70}$	%	f_t of the outer regions of the satellite above 70% of its radius (roughly $\frac{2}{3}$ by mass)
13	$f_t^{s,90}$	%	f_t of the outer regions of the satellite above 90% of its radius (roughly $\frac{1}{4}$ by mass)
14	f_t^p	%	f_t of the full planet
15	$f_t^{p,85}$	%	f_t of the planet outside of 0.85 $R_{\oplus}$ by radius (roughly $\frac{1}{2}$ by mass)
16	f_t^d	%	f_t of the debris disk

Notes. Table 1 is published in its entirety in the machine-readable format. A description of the fields in the online table is shown here for guidance regarding its form and content.

[a] The "type" notes the other parameters that are changed from the base scenario for the following subsets of simulations, as described in Section 2, within which the angle and speed are then varied: the number of particles, N (base 10^7); the spin angular momentum of the target or impactor, $L_{t,i}$ (base 0); the mass of the impactor, M_i (base 0.133 $M_{\oplus}$); and the surface temperature, T_s (base 2000 K).

(This table is available in its entirety in machine-readable form.)

ORCID iDs

J. A. Kegerreis https://orcid.org/0000-0001-5383-236X
S. Ruiz-Bonilla https://orcid.org/0000-0003-0925-9804
V. R. Eke https://orcid.org/0000-0001-5416-8675
R. J. Massey https://orcid.org/0000-0002-6085-3780
T. D. Sandnes https://orcid.org/0000-0002-4630-1840
L. F. A. Teodoro https://orcid.org/0000-0002-8346-0138

References

Asphaug, E. 2014, AREPS, 42, 551
Asphaug, E., Emsenhuber, A., Cambioni, S., Gabriel, T. S. J., & Schwartz, S. R. 2021, PSJ, 2, 200
Balsara, D. S. 1995, JCoPh, 121, 357
Benz, W., Slattery, W. L., & Cameron, A. G. W. 1987, Icar, 71, 30
Cameron, A. G. W., & Ward, W. R. 1976, LPSC, 7, 120
Cano, E. J., Sharp, Z. D., & Shearer, C. K. 2020, NatGe, 13, 270
Canup, R. 2008, Icar, 196, 518
Canup, R. M. 2012, Sci, 338, 1052
Canup, R. M., & Asphaug, E. 2001, Natur, 412, 708
Canup, R. M., Righter, K., Dauphas, N., et al. 2021, arXiv:2103.02045
Charlier, B., Grove, T. L., Namur, O., & Holtz, F. 2018, GeCoA, 234, 50
Citron, R. I., Manga, M., & Tan, E. 2018a, E&PSL, 491, 58
Citron, R. I., Perets, H. B., & Aharonson, O. 2018b, ApJ, 862, 5
Ćuk, M., Hamilton, D. P., Lock, S. J., & Stewart, S. T. 2016, Natur, 539, 402
Ćuk, M., & Stewart, S. T. 2012, Sci, 338, 1047
Dauphas, N. 2017, Natur, 541, 521
Dauphas, N., Nie, N. X., Blanchard, M., et al. 2022, PSJ, 3, 29
Day, J. M. D., van Kooten, E. M. M. E., Hofmann, B. A., & Moynier, F. 2020, E&PSL, 531, 115998
Deng, H., Ballmer, M. D., Reinhardt, C., et al. 2019a, ApJ, 887, 211
Deng, H., Reinhardt, C., Benitez, F., et al. 2019b, AJ, 870, 127
Desch, S. J., & Robinson, K. L. 2019, Geoch, 79, 125546
Genda, H., Fujita, T., Kobayashi, H., Tanaka, H., & Abe, Y. 2015, Icar, 262, 58
Goldreich, P., & Tremaine, S. 1980, ApJ, 241, 425
Hartmann, W. K., & Davis, D. R. 1975, Icar, 24, 504
Hosono, N., Iwasawa, M., Tanikawa, A., et al. 2017, PASJ, 69, 26
Hosono, N., Karato, S.-i., Makino, J., & Saitoh, T. R. 2019, NatGe, 12, 418
Johansen, A., Ronnet, T., Bizzarro, M., et al. 2021, SciA, 7, eabc0444
Johnson, T. E., Morrissey, L. J., Nemchin, A. A., Gardiner, N. J., & Snape, J. F. 2021, E&PSL, 556, 116721
Kegerreis, J. A., Eke, V. R., Gonnet, P., et al. 2019, MNRAS, 487, 1536
Kegerreis, J. A., Eke, V. R., Massey, R. J., & Teodoro, L. F. A. 2020, ApJ, 897, 161
Lock, S. J., Bermingham, K. R., Parai, R., & Boyet, M. 2020, SSRv, 216, 109
Lock, S. J., Stewart, S. T., Petaev, M. I., et al. 2018, JGRE, 123, 910
Mastrobuono-Battisti, A., & Perets, H. B. 2017, MNRAS, 469, 3597
Matsuyama, I., Trinh, A., & Keane, J. T. 2021, PSJ, 2, 232
Meier, M. M. M., Reufer, A., & Wieler, R. 2014, Icar, 242, 316
Melosh, H. J. 2014, PTRSA, 372, 20130168
Nakajima, M., & Stevenson, D. J. 2015, E&PSL, 427, 286
Pahlevan, K., & Morbidelli, A. 2015, Natur, 527, 492
Pahlevan, K., & Stevenson, D. J. 2007, E&PSL, 262, 438
Pritchard, M. E., & Stevenson, D. J. 2000, in Thermal Aspects of a Lunar Origin by Giant Impact, ed. R. M. Canup, K. Righter et al. (Tucson, AZ: Univ. Arizona Press), 179
Reufer, A., Meier, M. M. M., Benz, W., & Wieler, R. 2012, Icar, 221, 296
Rufu, R., Aharonson, O., & Perets, H. B. 2017, NatGe, 10, 89
Rufu, R., & Canup, R. M. 2020, JGRE, 125, e06312
Ruiz-Bonilla, S., Borrow, J., Eke, V. R., et al. 2022, MNRAS, 512, 4660
Ruiz-Bonilla, S., Eke, V. R., Kegerreis, J. A., Massey, R. J., & Teodoro, L. F. A. 2021, MNRAS, 500, 2861
Salmon, J., & Canup, R. M. 2012, ApJ, 760, 83
Schaller, M., Gonnet, P., Chalk, A. B. G., & Draper, P. W. 2018, ascl soft, ascl:1805.020
Schiller, M., Bizzarro, M., & Fernandes, V. A. 2018, Natur, 555, 507
Stewart, S. T., Davies, E. J., Duncan, M. S., et al. 2019, AIP Conf. Proc. 2272 (Melville, NY: AIP)
Tian, Z., & Wisdom, J. 2020, PNAS, 117, 15460
Tillotson, J. H. 1962, General Atomic Report, Technical Report, GA-3216, 141
Touma, J., & Wisdom, J. 1994, AJ, 108, 1943
Touma, J., & Wisdom, J. 1998, AJ, 115, 1653
Wadsley, J. W., Keller, B. W., & Quinn, T. R. 2017, MNRAS, 471, 2357
Ward, W. R., & Canup, R. M. 2000, Natur, 403, 741
Williams, J. G., Konopliv, A. S., Boggs, D. H., et al. 2014, JGR Planets, 119, 1546